Heliyon 9 (2023) e22415

Contents lists available at ScienceDirect

Heliyon

journal homepage: www.cell.com/heliyon

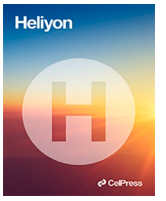

# Method of moments solution to ethylene glycol based $Al_2O_3$ nanofluid flow through expanding/contracting rectangular channel

Noor Muhammad, Naveed Ahmed *

*Department of Mathematics, Faculty of Sciences, HITEC University, Taxila, Pakistan*

ARTICLE INFO

*Keywords:*
Ethylene glycol
Rectangular channel
Permeable walls
Nanoparticle aggregation
Method of moments
Expanding contracting walls

ABSTRACT

In this study, we present a comprehensive analysis of the laminar time-dependent magnetohydrodynamic (MHD) flow of ethylene glycol-based aluminum oxide nanofluid through a rectangular channel with contracting/expanding porous walls. We investigate the influence of aggregation/non-aggregation of nanoparticles, as well as the presence of thermal radiation. By imposing self-similarities in space and time, we obtain a system of nonlinear ordinary differential equations governing the flow. To solve these equations, we employ a well-known semi-analytical technique known as the Method of Moments (MoM). Additionally, we compare our results with the outcomes achieved through an application of another commonly utilized numerical approach (shooting technique with the Runge-Kutta-Fehlberg scheme). The comparison shows an excellent agreement that endorses the accuracy of the calculated solutions. The velocity and temperature profiles obtained from our analysis exhibit variations due to the changes in involved dimensionless parameters. We present these variations through graphical representations along with their explanations. Interestingly, our study reveals that the aggregation of nanoparticles influences the fluctuations caused by other parameters, and to some extent, suppresses them. Consequently, we observe less deviation among the velocity and temperature curves for the aggregation case compared to the non-aggregation case. These findings have significant implications in real-world engineering and industry. The understanding of the flow behavior of nanofluids through expanding/contracting rectangular channels can aid in the design and optimization of various engineering systems, such as heat exchangers and microfluidic devices. Additionally, our study provides valuable insights into the effects of nanoparticle aggregation and thermal radiation in such systems, offering opportunities for enhancing their efficiency and performance.

## 1. Introduction

The fluid movement through flexible domains is useful for a variety of purposes in industrial and engineering processes like coolant transmission systems, cleaning and circulation processes, aerospace technology and inter-body transportation systems in living organisms, etc. Both the contractions and expansions play important roles in various fluid mechanics applications, such as pipe fittings, nozzles, diffusers, valves, and hydraulic systems. A comprehensive understanding of how fluids behave in these geometric transitions is

* Corresponding author.
*E-mail address:* nidojan@gmail.com (N. Ahmed).

https://doi.org/10.1016/j.heliyon.2023.e22415
Received 22 February 2023; Received in revised form 26 September 2023; Accepted 11 November 2023
Available online 19 November 2023

**Nomenclature**

| | |
|---|---|
| $\widetilde{u}$, $\widetilde{v}$ | velocity components, horizontal and vertical respectively |
| $\widetilde{x}$, $\widetilde{y}$ | Distance components, horizontal and vertical respectively |
| $\widetilde{T}$, $\widetilde{T}_l$, $\widetilde{T}_u$ | Fluid Temperature, Lower and Upper wall temperatures respectively |
| $\widetilde{t}$, $\widetilde{p}$ | Time and pressure respectively |
| $\rho_f$ | Effective density for base fluid |
| $\rho_{nf}$ | Effective density for nanofluid |
| $\rho_{agg}$ | Effective density for nanoparticle aggregation |
| $(Cp)_f$ | Specific heat for base fluid |
| $(Cp)_{nf}$ | Specific heat for nanofluid |
| $(Cp)_{agg}$ | Specific heat for nanoparticles aggregation |
| $\mu_f$ | Effective dynamic viscosity for base fluid |
| $\mu_{nf}$ | Dynamic viscosity for nanofluid |
| $\mu_{agg}$ | Effective dynamic viscosity of nanoparticles aggregation |
| $\sigma_f$ | Electric conductivity of base fluid |
| $\sigma_{nf}$ | Electric conductivity of nanofluid |
| $\sigma_{agg}$ | Electric conductivity of nanoparticles aggregation |
| $R_l$ | Lower wall Permeation Reynolds |
| $\delta_{nf}$ | Thermal diffusivity |
| $(\rho Cp)_{nf}$ | product of density and specific heat of nanoparticles |
| $A_u$ | Upper wall permeability |
| $A_l$ | Lower wall permeability |
| $k_f$ | Effective thermal conductivity of base fluid |
| $k_{nf}$ | Thermal conductivity of nanofluid |
| $k_{agg}$ | Effective thermal conductivity of nanoparticles aggregation |
| $a_k$ | Mean absorption constant |
| $\sigma^*$ | Stephen Boltzmann constant |
| $B_O$ | Strength of Magnetic field |
| $M$ | Magnetic strength parameter |
| $\alpha$ | deformation rate for channel walls |
| $q_{rad}$ | Thermal radiation |
| $Rd$ | Radiation strength parameter |
| $\varphi$ | Solid volume fraction for nanoparticles |
| $Pr$ | Prandtl numbers respectively |
| $S$ | Porosity parameter |
| $\theta_r$ | Walls and reference temperature's ratio |
| $\begin{pmatrix} f(\eta), \\ \theta(\eta) \end{pmatrix}$ | Non-dimensional functions for velocity and temperature profiles |
| $\eta$ | Dimensionless distance in vertical |
| $R$ | Upper wall Permeation Reynolds |
| $D$ | Fractal index for the solid nanoparticles |
| $(R_P, R_{agg})$ | Radii of primary and aggregated nanoparticles respectively |
| $\varphi_{max}$ | Maximum particle packing fraction |
| $\varphi_{int}$ | Intrinsic packing fraction of nanoparticles |

essential for maximizing the performance, efficiency, and safety of these systems. Uchida and Aoki [1] laid foundation for studying flows within contracting/expanding domains. Their seminal work provided a fantastic research avenue (by converting Navier-Stoke equations to a single ordinary differential equation) for investigators to carry out research in permeable channels with contracting/expanding walls. Taking contraction of the walls into account, Goto and Uchida [2] examined the flow in pipes and successfully studied the characteristics of viscosity and the pressure distribution during the flow. Dauenhauer and Majdalani [3] contributed jointly in studying the injection driven flow in a dilating channel. They established that the flow properties can be translated in the form of two non-dimensional parameters i.e., expansion parameter $\alpha$ and permeation Reynolds number $R$. They evaluated shear stress, streamlines and pressure distribution as functions of space and time. Majdalani et al. [4] presented asymptotic solution for the flow between a permeable channel. They removed the overly imposed simplification assumptions made by Bhatnagar [5] and many other researchers. The behavior of large injection/suction in dilating and sequencing walls was also studied by Majdalani and Zhou [6]. Ahmed et al. [7] offered a finite element analysis for the flow in an expanding and squeezing permeable channel. Noor

and Naveed [8] carried out a semi-analytical investigation of the flow of $ZnO - SAE50$ nanolubricant in a horizontal asymmetrical porous channel with walls that expand and contract.

The significance of understanding fluid motion in daily life has increased greatly due to the flow of different fluids over diverse surfaces and their unique structures. This has led to significant advancements in various specialized fields for the research community. In recent years, nano-fluidic flow nanotechnology has gained significant importance due to improved thermal properties. The heat capacity of fluids can be improved by incorporating various nanoparticles into base fluids, such as ethylene glycol, water, and engine oils. The metallic and non-metallic thermophysical properties of nanosized particles are the driving force behind nanofluidic technology. Researchers are currently exploring the use of these properties in efficient heat exchangers for microchips, nuclear reactors, engines as coolants, and other nanometer-sized equipment, including their nitrides, carbides, and oxides. Numerous researchers have conducted extensive investigations into the vast array of potential applications for nanofluids within various industrial and engineering domains. For instance, the pioneering work of Choi and Eastman [9] was centered on the augmentation of thermal conductivity within fluids through the incorporation of nanoparticles. Simultaneously, Xuan and Li [10] delved deeply into the exploration of convective heat transfer characteristics and flow behaviors specific to nanofluids. Additionally, Buongiorno's contributions [11] have provided valuable insights into the intricate convective transport phenomena exhibited by nanofluids. Furthermore, Khan et al. [12] have expanded the scope of their investigations to clarify the intricate nonlinear radiation effects on the magnetohydrodynamic (MHD) flow of nanofluids over a nonlinearly stretching/shrinking wedge. The work of Basit et al. [13] has propelled advancements in thermal performance by harnessing the potential of multi-walled carbon nanotubes (MWCNTs) in water-based nanofluids, particularly in the context of shell and helical coil heat exchangers.

Aggregation in nanoparticles refers to the process of two or more particles coming together and forming clusters or aggregates. This can occur due to various factors, including electrostatic forces, van der Waals forces, hydrogen bonding, and hydrophobic interactions. The process of aggregation can alter the physical and chemical properties of nanoparticles, such as size, shape, surface area, stability, and bioavailability. These properties of aggregation lead an unusual moment of heat in nanoparticles. Also, many rheological and thermal properties in fluid flow problems are affected under the impact of nanoparticles aggregation. Motlagh and Kalteh [14] investigated the heat transportation in a nanochannel and concluded that nanoparticle velocity is exaggerated in presence of nanoparticle aggregation. Joule heating and nanoparticles aggregation effects on fluid flow were analyzed by Swain and Mahanthesh [15]. Mahanthesh et al. [16] also explored the heat transfer in the context of the flow of nanoparticle aggregation. Sabu et al. [17] opted for an inclined flat surface to investigate the motion characteristics of nanoparticle aggregation. Many other investigators like Wang et al. [18,19], Benos et al. [20], Sunthrayuth et al. [21], Acharya et al. [22], Ellahi et al. [23], Mackolil and Mahanthesh [24,25] published their work with useful experimental study for nanoparticles aggregation flow phenomena.

Thermal radiation deals with the expulsion of electromagnetic beams over a hot surface to the adjacent region in every direction. The thermal rays belonging to each object travel towards their respective points of absorption at a speed of light. Thermal radiation is important in many applications such as in the design of power plants, solar panels, and the insulation of buildings. By understanding the principles of thermal radiation, engineers can design systems that minimize heat loss and maximize energy efficiency. Kothandapania and Prakash [26] investigated the thermal radiations impact upon peristaltic motion in an asymmetric channel. They explored their research work for the Williamson fluid flow mechanism. Narayana et al. [27] studied electrically conducting fluid flow in a vertical and permeable system. They analyzed the thermal radiation execution and heat propagation for a mixed convection incompressible viscous flow. Naveed et al. [28] described the thermal radiation impression upon viscous fluid flow for a deformable channel. They conducted their study on a horizontal porous channel of asymmetrical nature. Anil Kumar et al. [29] improved the understating of rotating fluid flow for Hall current and radiation impacts in a vertical column. Adnan et al. [30] discussed the solar thermal radiations effects in Magnesium Zinc–Zirconium engine oil for three dimensional convectively heated surface. Recently, Saha et al. [31,32] investigated the effect of obstruction size and position on buoyancy-driven convection in a concentric annulus. They also explored how the shape of the obstructions (square and circular) influenced the thermal performance of the system.

The branch of science known as Magnetohydrodynamics (MHD) focuses on the examination of fluid flows that are electrically conductive and affected by magnetic fields. In such cases, the impact of magnetic fields on the fluid flow must be taken into consideration when modeling the flow. In industries MHD is used to improve thermal conductivity of the fluids. This combination of magnetic fields and fluid flow is critical due to its utilization in numerous technological devices such as nuclear reactors, MHD generators and MHD pumps. These engineered fluids do also have a variety of applications in engineering and medicine, including cooling processes, heat exchangers and drug delivery systems. Numerous studies by various researchers [33–40] have emphasized the significance of MHD flows in fields such as meteorology, solar physics, geophysics and even in industries and medicine.

After the innovative work described above, there have been numerous research efforts presenting the diverse characteristics of fluid behavior through the contracting and expanding permeable channels. However, no one has ever attempted to examine the aluminum oxide - ethylene glycol-based flow incorporating aggregation properties within a dilating and squeezing channel of porous walls that too under the impact of magnetic field and thermal radiation. Understanding the effects of nanoparticle aggregation is important for the design and optimization of engineering systems, such as heat exchangers and microfluidic devices, where nanofluids are utilized. By studying the behavior of nanofluids with aggregated nanoparticles, researchers can gain valuable insights into improving the efficiency and performance of such systems. Thus, to bridge this research gap, we have modeled this problem by applying the relevant conservation laws, so that we achieve a system of nonlinear partial differential equations which is further reduced to a system of nonlinear ordinary differential using similarity transformations. The solution of the problem is then obtained through a well-known semi-analytical technique labeled as Method of Moments. Besides this, shooting technique along with Runge-Kutta-Fehlberg (RKF) scheme is also employed and the results are found in an excellent agreement. The nanoparticles flow behavior and heat transfer properties are expressed through graphs and tables. A comprehensive study for aggregation and non-aggregation phenomena has also

been carried out to explain the impact of different significant physical factors in the field geometric concepts.

## 2. Formulation of problem

We have analyzed the aluminum oxide - ethylene glycol-based fluid flow through expanding contracting walls within a rectangular channel. Aluminum oxide $Al_2O_3$ is a chemical compound of aluminum $Al_2$ and oxygen $O_3$, which is commonly used in different chemical and industrial processes [41–43]. The base fluid ethylene glycol $(CH_2OH)_2$ is a colorless and odorless raw substantial biological carbon bounding which is frequently used as an antifreeze lubricant as well as in many other man-made industrial and domestic organic materials [44]. On the other hand, geometrically the movement of the channel's walls are either away or towards each other. That is, the height of the channel $a(t)$ varies exhibiting squeezing or dilating motion. In conjunction with the motion of the upper and lower walls of the channel, the leading edge (which is covered with a stretchable nonpermeable membrane) also exhibits a synchronized motion. The walls of the channel are permeable and nanofluid is permitted to be injected in. The problem is modeled for aggregation and non-aggregation phenomena along with the injunction aspects. The geometric development of the problem is characterized in the subsequent (Fig. 1).

The central point of the leading membrane is considered as the origin and the center line of the channel is taken as the positive x axis. The upper and the lower walls' temperatures are termed as $T_u$ and $T_l$ respectively. Furthermore, the walls have different permeabilities and we have applied a uniform magnetic force which is normal to the lower wall of the channel. On the other hand, we have also taken into account the radiative fluxes while modeling the energy equation.

Under aforementioned assumptions, the mathematical formulation of the problem can be listed as follows: [2,6].

$$\frac{\partial \widetilde{u}}{\partial \widetilde{x}}+\frac{\partial \widetilde{v}}{\partial \widetilde{y}}=0, \tag{1}$$

$$\frac{\partial \widetilde{p}}{\partial \widetilde{x}}=\mu_{nf}\left(\begin{array}{c}\frac{\partial^2 \widetilde{u}}{\partial \widetilde{x}^2}\\ +\frac{\partial^2 \widetilde{u}}{\partial \widetilde{y}^2}\end{array}\right)-\rho_{nf}\left(\begin{array}{c}\frac{\partial \widetilde{u}}{\partial \widetilde{t}}\\ +\widetilde{u}\frac{\partial \widetilde{u}}{\partial \widetilde{x}}\\ +\widetilde{v}\frac{\partial \widetilde{u}}{\partial \widetilde{y}}\end{array}\right)-\sigma_{nf}B_o^2\widetilde{u}, \tag{2}$$

$$\frac{\partial \widetilde{p}}{\partial \widetilde{y}}=\mu_{nf}\left(\frac{\partial^2 \widetilde{v}}{\partial \widetilde{x}^2}+\frac{\partial^2 \widetilde{v}}{\partial \widetilde{y}^2}\right)-\rho_{nf}\left(\frac{\partial \widetilde{v}}{\partial \widetilde{t}}+\widetilde{u}\frac{\partial \widetilde{v}}{\partial \widetilde{x}}+\widetilde{v}\frac{\partial \widetilde{v}}{\partial \widetilde{y}}\right), \tag{3}$$

$$\frac{\partial \widetilde{T}}{\partial \widetilde{t}}+\widetilde{u}\frac{\partial \widetilde{T}}{\partial \widetilde{x}}+\widetilde{v}\frac{\partial \widetilde{T}}{\partial \widetilde{y}}=\delta_{nf}\left(\frac{\partial^2 \widetilde{T}}{\partial \widetilde{x}^2}+\frac{\partial^2 \widetilde{T}}{\partial \widetilde{y}^2}\right)-\frac{1}{(\rho C_p)_{nf}}\left(\frac{\partial}{\partial \widetilde{x}}+\frac{\partial}{\partial \widetilde{y}}\right)q_{rad}, \tag{4}$$

here, Eq. (1) is mass conservation law, Eqs. ((2)–(3)) represent momentum conservation law and Eq. (4) expresses energy conservation law.

The heat flux $q_{rad}$ in Eq. (4) is due to the thermal radiation and it can be expressed in terms of the following Rosseland approximation [45,46].

$$q_{\mathrm{rad}}=\frac{4\sigma^*\widetilde{T}^3}{3a_k}\frac{\partial \widetilde{T}}{\partial \widetilde{y}}, \tag{5}$$

Eq. (5) shows that the radiative flux can be expressed as a function of temperature $\widetilde{T}$ and the temperature gradient $\left(\frac{\partial \widetilde{T}}{\partial \widetilde{y}}\right)$. In the same equation, $\sigma^*$ represents the Stefan–Boltzmann constant and $a_k$ stands for the average absorption constant.

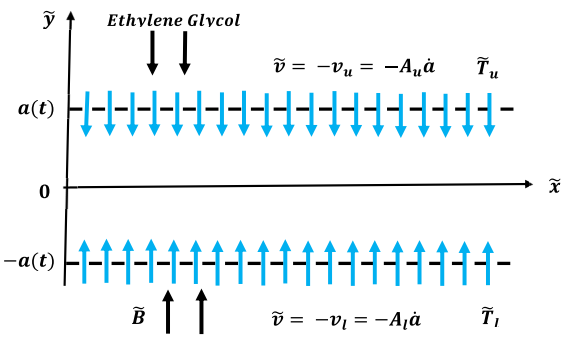


**Fig. 1.** Physical flow diagram.

The associated boundary conditions can be outlined as follows:

$$\widetilde{u}=0,\widetilde{v}=-\widetilde{v}_l=-A_l\dot{a},\widetilde{T}=\widetilde{T}_l \text{at} \widetilde{y}=-a(\widetilde{t}), \tag{6}$$

$$\widetilde{u}=0,\widetilde{v}=-\widetilde{v}_u=-A_u\dot{a},\widetilde{T}=\widetilde{T}_u \text{at} \widetilde{y}=a(\widetilde{t}). \tag{7}$$

Eqs. (6) and (7) are the boundary conditions specifying the velocity and temperature values at the lower and upper walls of the channel, respectively. Moreover, $\widetilde{u}$ and $\widetilde{v}$ are the components of velocity in the direction of $\widetilde{x}$ and $\widetilde{y}$, respectively. Moreover, $B_0$ is magnetic field, $\widetilde{p}$ is pressure, $\widetilde{T}$ is the temperature of fluid, $\widetilde{T}_u$ is the temperature of upper wall, $\widetilde{T}_l$ is the temperature of lower wall, $A_u$ is the upper wall's permeability and $A_l$ is the lower wall's permeability.

Additionally, the expressions for various physical properties of the nanoparticles like effective dynamic viscosity $\mu_{nf}$, effective density $\rho_{nf}$, electric conductivity $\sigma_{nf}$, thermal diffusivity $\delta_{nf}$, effective thermal conductivity $k_{nf}$ and the product of density and specific heat $(\rho Cp)_{nf}$ are given in Eqs. ((8)–(18)). These equations incorporate the aggregation behavior of nanoparticles and the properties of the base fluid and solid nanoparticles (Ref. [18,23]).

$$\mu_{nf}=\mu_f\left(1-\frac{\varphi_{agg}}{\varphi_{max}}\right)^{-\frac{5}{2}*\varphi_{max}}, \tag{8}$$

$$\rho_{nf=}\left(1-\varphi_{agg}\right)\rho_f+\varphi_{agg}\rho_{agg}, \tag{9}$$

$$\sigma_{nf}=\sigma_f\left[1+\frac{3\left(\frac{\sigma_s}{\sigma_f}-1\right)\varphi_{agg}}{\left(\frac{\sigma_s}{\sigma_f}+2\right)-\left(\frac{\sigma_s}{\sigma_f}-1\right)\varphi_{agg}}\right] \tag{10}$$

$$\delta_{nf}=\frac{k_{nf}}{(\rho Cp)_{nf}} \tag{11}$$

$$k_{nf}=k_f\left[\frac{k_{agg}+2k_f+2\varphi_{agg}\left(k_{agg}-k_f\right)}{k_{agg}+2k_f-\varphi_{agg}\left(k_{agg}-k_f\right)}\right] \tag{12}$$

$$(\rho Cp)_{nf}=\left(1-\varphi_{agg}\right)(\rho Cp)_f+\varphi_{agg}(\rho Cp)_{agg}, \tag{13}$$

$$\varphi_{agg}=\frac{\varphi}{\varphi_{int}}, \tag{14}$$

$$\varphi_{int}=\left(\frac{R_{agg}}{R_P}\right)^{D-3} \tag{15}$$

$$\rho_{agg}=(1-\varphi_{int})\rho_f+\varphi_{int}\rho_s, \tag{16}$$

$$(\rho Cp)_{agg}=(1-\varphi_{int})(\rho Cp)_f+\varphi_{int}(\rho Cp)_s, \tag{17}$$

$$\mathrm{k_{agg}}=\frac{\mathrm{k_f}}{4}\left[(3\varphi_{\mathrm{int}}\text{-}1)\frac{\mathrm{k_s}}{\mathrm{k_f}}+\{3(1\text{-}\varphi_{\mathrm{int}})\text{-}1\}+\left[\left\{(3\varphi_{\mathrm{int}}\text{-}1)\frac{\mathrm{k_s}}{\mathrm{k_f}}+(3(1\text{-}\varphi_{\mathrm{int}})\text{-}1)\right\}^2+\frac{8\mathrm{k_s}}{\mathrm{k_f}}\right]^{\frac{1}{2}}\right] \tag{18}$$

From fractal theory the above equations described that $\varphi_{max}$ represents the maximum particle packing fraction and it has a fixed value 0.605 for the shape of spherical bodies. Furthermore $R_P$ and $R_{agg}$ are the radii of primary nanoparticles and radii of aggregation respectively, with the ratio $\frac{R_{agg}}{R_P}=3.34$ and $D$ is the fractal index having value 1.8 for the solid nanoparticles. Furthermore, by setting $\varphi_{int}=1.0$, $\varphi_{agg}$ becomes equal to $\varphi$ and with further assumption $\varphi_{max}=1.0$, leads our calculations towards nanoparticles non-aggregation scenario.

We have cross-differentiated Eqs. (2) and (3) to get rid of the pressure gradient term, Eq. (19) shows the consequent equation that is:

$$\begin{aligned}&\mu_{nf}\left(\frac{\partial^3\widetilde{u}}{\partial\widetilde{x}^2\partial\widetilde{y}}+\frac{\partial^3\widetilde{u}}{\partial\widetilde{y}^3}\right)-\rho_{nf}\left(\frac{\partial^2\widetilde{u}}{\partial\widetilde{t}\partial\widetilde{y}}+\widetilde{u}\frac{\partial^2\widetilde{u}}{\partial\widetilde{x}\partial\widetilde{y}}+\frac{\partial\widetilde{u}}{\partial\widetilde{x}}\frac{\partial\widetilde{u}}{\partial\widetilde{y}}+\widetilde{v}\frac{\partial^2\widetilde{u}}{\partial\widetilde{y}^2}+\frac{\partial\widetilde{u}}{\partial\widetilde{y}}\frac{\partial\widetilde{v}}{\partial\widetilde{y}}\right)-\sigma_{nf}B_\circ^2\frac{\partial\widetilde{u}}{\partial\widetilde{y}}\\&=\mu_{nf}\left(\frac{\partial^3\widetilde{v}}{\partial\widetilde{y}^2\partial\widetilde{x}}+\frac{\partial^3\widetilde{v}}{\partial\widetilde{x}^3}\right)-\rho_{nf}\left(\frac{\partial^2\widetilde{v}}{\partial\widetilde{t}\partial\widetilde{x}}+\widetilde{u}\frac{\partial^2\widetilde{v}}{\partial\widetilde{x}^2}+\frac{\partial\widetilde{v}}{\partial\widetilde{x}}\frac{\partial\widetilde{u}}{\partial\widetilde{x}}+\widetilde{v}\frac{\partial^2\widetilde{v}}{\partial\widetilde{x}\partial\widetilde{y}}+\frac{\partial\widetilde{v}}{\partial\widetilde{y}}\frac{\partial\widetilde{v}}{\partial\widetilde{x}}\right).\end{aligned} \tag{19}$$

After formulating the mathematical equations, we proceed to simplify them by introducing non-dimensional variables and transformations, which are listed in Eq. (20). This simplification leads to a set of non-linear ordinary differential equations in a non-

dimensional form.

$$\eta = \frac{\widetilde{y}}{a(\widetilde{t})}, \quad \widetilde{u} = \frac{\vartheta_f \, \widetilde{x} \, \overline{f}_\eta(\eta,\widetilde{t})}{a^2(\widetilde{t})}, \quad \widetilde{v} = -\frac{\vartheta_f \overline{f}(\eta,\widetilde{t})}{a(\widetilde{t})}, \quad \theta(\eta) = \frac{\widetilde{T} - \widetilde{T}_u}{\widetilde{T}_l - \widetilde{T}_u}. \tag{20}$$

So that, the equation of continuity is satisfied identically and the remaining momentum and energy equations gross the subsequent arrangement:

$$\overline{f}_{\eta\eta\eta\eta} + \frac{\vartheta_f}{\vartheta_{nf}} \left( \alpha \begin{pmatrix} 3\overline{f}_{\eta\eta} \\ +\eta\overline{f}_{\eta\eta\eta} \end{pmatrix} - \overline{f}_\eta \overline{f}_{\eta\eta} + \overline{f}\overline{f}_{\eta\eta\eta} \right) - \overline{f}_{\eta\eta} M D_1 D_2 - \frac{a^2 \, \overline{f}_{\eta\eta\widetilde{t}}}{\vartheta_{nf}} = 0, \tag{21}$$

The parameter $\alpha = a\dot{a}/\vartheta_f$ in Eq. (21) expressed the wall deformation rate and its negative and positive values are corresponded to contraction and expansion respectively. To accomplish a self-similar result for time, we may take $\alpha$ to be a constant and $\overline{f}$ to be purely a function of $\eta$ that in turn allows us to remove the term $\overline{f}_{\eta\eta\widetilde{t}}$, (See. Uchida and Aoki [47] as well as Majdalani and Zhou [6]). The value of $\alpha$ may be calculated on the basis of initial height of the channel $a_0$ and the dilation rate $\dot{a}_0$.

Following the same assumption, the energy equation leads to:

$$-\frac{k_{nf}}{k_f}\theta_{\eta\eta} - \mathrm{Pr}\frac{(\rho Cp)_{nf}}{(\rho Cp)_f}(\alpha\eta + \overline{f}R)\theta_\eta + \mathrm{Rd}\left[\{1 + (\theta_r\text{-}1)\theta(\eta)\}^3\theta_{\eta\eta} + 3\left(\{1 + (\theta_r\text{-}1)\theta(\eta)\}^2\right)(\theta_r\text{-}1)(\theta_\eta)^2\right] = 0. \tag{22}$$

Now the boundary conditions can be written as:

$$\begin{aligned} &\overline{f}(\eta)|_{\eta=-1} = R_l, \overline{f}_\eta(\eta)|_{\eta=-1} = 0, \theta(\eta)|_{\eta=-1} = 1, \\ &\overline{f}(\eta)|_{\eta=1} = R, \overline{f}_\eta(\eta)|_{\eta=1} = 0, \theta(\eta)|_{\eta=1} = 0, \end{aligned} \tag{23}$$

here for the lower and upper walls, the permeation Reynolds numbers are $R_l = \frac{\widetilde{v}_l a}{\vartheta_f}$ and $R = \frac{\widetilde{v}_u a}{\vartheta_f}$, respectively. For injection situation, we have considered the positive values of the Reynolds number.

The governing Eqs. (21) and (22) strengthen with boundary conditions (23) are further simplified using the following scale variables to enhance their clarity and applicability.

$$\overline{u} = \dot{a}^{-1}u, \overline{v} = \dot{a}^{-1}v, \overline{x} = \dot{a}^{-1}x, \overline{f} = fR \tag{24}$$

Hence, introducing Eq. (24), we finally obtain a non-dimensional form for the governing equations related to momentum and energy in the form nonlinear ODEs as follows:

$$f^{(iv)} + r_1\{\alpha(3f'' + \eta f''') - R(f'f'' - ff'')\} - f''RMD_1D_2 = 0 \tag{25}$$

$$\mathrm{r}_3\,\theta'' + \mathrm{Pr}\,\mathrm{r}_2(\alpha\eta + \mathrm{fR})\theta' - \mathrm{Rd}\left[\{1 + (\theta_r - 1)\theta\}^3\theta'' + 3\left(\{1 + (\theta_r - 1)\theta\}^2\right)(\theta_r - 1)\theta'^2\right] = 0 \tag{26}$$

with dimensionless boundary conditions:

$$\begin{aligned} &f(\eta) = \mathrm{S}, f'(\eta) = 0, \theta(\eta) = 1, \text{for}\eta = -1 \\ &f(\eta) = 1, f'(\eta) = 0, \theta(\eta) = 0, \text{for}\eta = 1. \end{aligned} \tag{27}$$

Furthermore, in above equations we have,

$$r_1 = \frac{\vartheta_f}{\vartheta_{nf}} = \left(1 - \frac{\varphi_{agg}}{\varphi_{max}}\right)^{\frac{5}{2}*\varphi_{max}} \left[1 - \varphi_{agg} + \varphi_{agg}\left(\frac{\rho_{agg}}{\rho_f}\right)\right] \tag{28}$$

$$\alpha = \frac{a\dot{a}}{\vartheta_f}, \tag{29}$$

$$R = \frac{\widetilde{V}_u a}{\vartheta_f}, \tag{30}$$

$$M = \frac{\sigma_f B_0{}^2 a^2}{\rho_f \, \vartheta_f} \tag{31}$$

$$D_1 = \frac{\sigma_{nf}}{\sigma_f} = \left[1 + \frac{3\left(\frac{\sigma_s}{\sigma_f} - 1\right)\varphi_{agg}}{\left(\frac{\sigma_s}{\sigma_f} + 2\right) - \left(\frac{\sigma_s}{\sigma_f} - 1\right)\varphi_{agg}}\right] \tag{32}$$

$$D_2 = \left(1 - \frac{\varphi_{agg}}{\varphi_{max}}\right)^{\frac{5}{2}*\varphi_{max}} \tag{33}$$

$$r_2 = \frac{(\rho Cp)_{nf}}{(\rho_{Cp})_f} = \frac{(1-\varphi_{agg})(\rho Cp)_f + \varphi_{agg}(\rho Cp)_{agg}}{(\rho_{Cp})_f} \tag{34}$$

$$r_3 = \frac{k_{nf}}{k_f} = \left[\frac{k_{agg}+2k_f+2\varphi_{agg}(k_{agg}-k_f)}{k_{agg}+2k_f-\varphi_{agg}(k_{agg}-k_f)}\right] \tag{35}$$

$$Pr = \frac{\vartheta_f}{\delta_f} = \frac{\mu_{f/}\rho_f}{k_f/(\rho Cp)_f} = \frac{\mu_f (Cp)_f}{k_f} \tag{36}$$

$$Rd = \frac{4\sigma^* \widetilde{T}_u^3}{3a_k k_f} \tag{37}$$

$$\theta_r = \frac{\widetilde{\theta}_l}{\widetilde{\theta}_r} \tag{38}$$

$$S = \frac{v_l}{v_u} \tag{39}$$

The skin friction coefficient $C_f$ and local Nusselt number $Nu$ are required physical quantities of interest which are presented as:

$$C_f = \frac{a(t)T_w}{\rho_{nf}\widetilde{V}_l^{\,2}x} \tag{40}$$

$$T_w = \mu_{nf}\left(\frac{\partial \mathrm{u}}{\partial \mathrm{y}}\right)_{y=\pm a(t)} \tag{41}$$

where the skin friction in non-dimensional form for upper and lower walls is given as:

$$C_f {R_l}^2 = \frac{\left(1 - \frac{\varphi_{agg}}{\varphi_{max}}\right)^{-\frac{5}{2}*\varphi_{max}}}{(1-\varphi_{agg})\rho_f + \varphi_{agg}\rho_{agg}} f''(-1) \tag{42}$$

$$C_f {R_u}^2 = \frac{\left(1 - \frac{\varphi_{agg}}{\varphi_{max}}\right)^{-\frac{5}{2}*\varphi_{max}}}{(1-\varphi_{agg})\rho_f + \varphi_{agg}\rho_{agg}} f''(1) \tag{43}$$

$$Nu = -\frac{a}{k_f(\widetilde{T}_l - \widetilde{T}_u)}\left(k_{nf}\frac{\partial \widetilde{T}}{\partial \mathrm{y}} + q_{rad}\right)_{y=\pm a(t)} \tag{44}$$

here, the nondimensional case of local Nusselt for lower and upper walls is as listed below:

$$Nu_{lower} = -\theta'(-1)[\mathrm{r}_3 + \mathrm{Rd}\{1+(\theta_\mathrm{r}-1)\theta(-1)\}^3], \tag{45}$$

$$\mathrm{Nu}_{\mathrm{upper}} = -\theta'(1)[r_3 + Rd\{1+(\theta_r-1)\theta(1)\}^3] \tag{46}$$

Table 1, displays the thermo-physical properties of the base fluid ethylene glycol and nanoparticles aluminum oxide ($Al_2O_3$) .

**Table 1**
Thermo-physical properties of base fluid ethylene glycol and nanoparticles aluminum oxide ($Al_2O_3$) [25,48].

| Fluid | $\sigma$ /(oh $m^{-1}.cm^{-1}$) | $P$ /(kg/ $m^3$) | $C_p$ /(J/(kg.K)) | $K$ /(W/mK) | $\mu_f$ /(Ns/ $m^2$) | $Pr$ |
|---|---|---|---|---|---|---|
| Ethylene Glycol | $1.07 \times 10^{-6}$ | 1114 | 2415 | 0.252 | 0.0157 | 204 |
| $Al_2O_3$ | $35 \times 10^6$ | 3970 | 765 | 40 | – | – |

## 3. Solution methodologies for presented problem

The solution of the flow problem is initially calculated through a semi analytical procedure named as Method of Moments (MoM) [49–51]. MoM is a subdivision of the trial-based solution (generally a linear combination of orthonormal basis) of weighted residual process [52]. The Method of Moments (MoM) is a semi-analytical technique used to solve differential equations by transforming them into algebraic equations. It involves expressing the unknown solution as a trial function with adjustable parameters and minimizing the deviation between the trial solution and the actual solution through a weighted residual function. By equating the weighted residuals to zero, a system of algebraic equations is obtained, and solving these equations provides the values of the parameters. The resulting values are used to construct an approximate solution for the original differential equation. The MoM is a versatile and efficient method for semi analytical solutions when pure analytical solutions are unavailable, offering reasonable accuracy and finding applications in various scientific and engineering domains. The basic methodology of this technique can be outlined as follows.

### 3.1. Method of moments (MoM)

In order to understand how the MoM operates, we consider an ordinary differential equation as follows:

$$D(v(x)) = f(x), \tag{47}$$

along with associated initial and boundary conditions specified upon the domain Ω. Eq. (47) expresses a transformation of the depended variable $v(x)$ under the differential operator $D$ to a source function $f(x)$.

To solve Eq. (47), we propose the following trial solution $\widetilde{v}(x)$ for the estimation of the actual solution ($v(x)$),

$$v(x) \cong \widetilde{v}(x) = c_0 + \sum_{i=1}^{n} c_i.(x)^i \tag{48}$$

where, $c_i s$ are the constants to be computed and $(x)^i, i = 1, 2, 3, \ldots\ldots, n$ are the basis functions for trial solution $\widetilde{v}(x)$. This trial solution in Eq. (48) itself becomes the numerical solution of the flow problem if it satisfies the differential equation (47) as well as the associated boundary condition. However, this ideal situation is a very rare feast, mostly it drops a nonzero error which is termed as residue function. The residue function can be expressed as follows:

$$R(x) = D(v(x)) - f(x) \neq 0 \tag{49}$$

In MoM, Firstly, a weighted residual is calculated and then it is set equal to zero. The associated mathematical expression is as follows

$$\int_{\Omega} R(x)\ w_i(x) dx = 0, \text{where} i = 1, 2, 3, \ldots\ldots, n. \tag{50}$$

Using Eq. (49) in Eq. (50), setting the weights $w_i(x) = (x)^{i-1}$ and integrating the weighted residual function $R(x)$, we get a system of algebraic equations in constants $c_i s$. The obtained system of these algebraic equations coupled with the boundary residue is used to find the unknown parameters $c_i$ s that fit the trial solution to the actual solution of the differential equation. In the Method of Moments approach, $c_i$ s represents the coefficients of the trial solutions for the unknown functions and they are crucial in obtaining an approximate semi-analytical solution for the flow problem

For the application of MoM to solve the differential equations of our flow model (Eqs. (25)–(27)), we need two trial solutions enlisted the following equations:

$$\widetilde{f}(\eta) = b_0 + \sum_{i=0}^{n} b_i.(\eta)^i. \tag{51}$$

$$\widetilde{\theta}(\eta) = c_0 + \sum_{i=0}^{n} c_i.(\eta)^i \tag{52}$$

To obtain the estimated solution for these trial functions of velocity and temperature, the set of values for different parameters is given as follows:

$$\varphi = 0.01, \alpha = -1.5, \mathrm{R} = 2.5, \mathrm{S} = -0.5, \mathrm{Pr} = 204, \mathrm{M} = Rd = 2.0. \tag{53}$$

We use Eqs. (51)–(53) along with the thermophysical values in the differential equation and associated conditions to get the residual functions and boundary residues. Preceding in a similar manner as stated above, we get the values of the paraments by setting weighted residuals and boundary residues to zero. Consequently, we get the solutions for both aggregation and non-aggregation cases (mentioned in Eqs. (54) to (57)).

For aggregation case:

$$f(\eta) \cong \widetilde{f}(\eta) = 0.280063953199712223 + 1.03938794887239006\eta - 0.0475767932384262085\eta^2 - 0.210844335149987017\eta^3 + 0.00606137528892755455\eta^4 - 0.0713696226931195415\eta^5 + 0.0103221032595379701\eta^6 - 0.00722229027386543480\eta^7 + 0.00113737358761714000\eta^8 + 4.353437340828516\times10^{-6}\eta^9 + 0.000013721669200896 5\eta^{10} + 0.0000306289267682878\eta^{11} - 0.000021718444191216\eta^{12} + 0.0000133156460108096\eta^{13} \quad (54)$$

$$\theta(\eta) \cong \widetilde{\theta}(\eta) = -0.396166594169481412 + 0.639653674918008952\eta - 0.638826987718520867\eta^2 + 0.513374222223433985\eta^3 + 1.81803594512245126\eta^4 - 5.47286908105276471\eta^5 + 1.18607008293718508\eta^6 + 8.64707176299851987\eta^7 - 3.53335692601418128\eta^8 - 7.81742142386972549\eta^9 + 2.52540259743046658\eta^{10} + 4.02738687364134762\eta^{11} - 0.461158117588744643\eta^{12} - 1.03719602874209205\eta^{13} \quad (55)$$

For non-aggregation case,

$$f(\eta) \cong \widetilde{f}(\eta) = 0.281120592806166414 + 1.04351934374885813\eta - 0.0500204873393566771\eta^2 - 0.217951112999000884\eta^3 + 0.00757639187308564634\eta^4 - 0.0694669251074084698\eta^5 + 0.0103821586982916474\eta^6 - 0.00623379865628652732\eta^7 + 0.000964657891009654 0\eta^8 + 0.000088278098349486 24\eta^9 - 2.474230332673914\times10^{-6}\eta^{10} + 0.0000320328743177 7\eta^{11} - 0.000020838854607505\eta^{12} + 0.000012180578422370\eta^{13} \quad (56)$$

$$\theta(\eta) \cong \widetilde{\theta}(\eta) = -0.394334454672910839 + 0.636377861956445745\eta - 0.652963956793501610\eta^2 + 0.589785078953396269\eta^3 + 1.73841601984538530\eta^4 - 5.64493528263193145\eta^5 + 1.47830707524628902\eta^6 + 8.83230408812593559\eta^7 - 3.91499999511738439\eta^8 - 7.94397603080290349\eta^9 + 2.74968477803897393\eta^{10} + 4.09102385247486033\eta^{11} - 0.504109466547563057\eta^{12} - 1.06057956794350172\eta^{13} \quad (57)$$

For the other sets of values of the physical parameters, their respective solutions expressions can be obtained by repeating the same procedure. To double check the accuracy of the solutions, we employ another scheme which is purely numerical and it is in fact a couple of two different techniques that is Shooting method and Runge Kutta Fehlberg algorithm.

In the following tables a comparison between the results of both the methodologies is constructed. In aggregation case, velocity profile is discussed in Table 2 while Table 3 is listed for temperature profile. For non-aggregation case, we have constructed Table 4 and Table 5 for velocity and temperature profiles respectively. All the comparative tables indicate an excellent agreement between both the solutions. It raises our confidence further that the solutions are correct.

## 4. Results and discussion

In this section we have penned down the physical outcomes of the flow characteristics for different sets of the values of the parameters involved. The relevant parameters are deformation rate for walls α, permeation Reynolds number $R$, magnetic strength parameter M, porosity parameter S, $Al_2O_3$ volume fraction φ and thermal radiation Rd. For the illustration of aggregation and non-aggregation phenomena, we take two scenarios: one with nanoparticles aggregation ($\varphi_{int} \neq 1$, green solid lines in the plots) and the other without nanoparticles aggregation ($\varphi_{int} = 1$, black dashed lines in the plots). Moreover, the observations are made for both dilating and squeezing cases, together with injection, for both velocity and temperature profiles against the various parameters. The plots related to the velocity are given in the figures Fig. 2 - Fig. 12, while for the temperature distribution Fig. 13 - Fig. 23 are displayed. Furthermore, at the end of this section, we have plotted the graphs for local Nusselt numbers at both the upper and lower walls (see Fig. 24 - Fig. 27).

We first focus on discussing the velocity profile under the impacts of contraction and expansion. The terms “contraction” and “expansion” refer to the decrease and increase in the height of the channel, respectively. We have constructed Fig. 2 for contraction ($\alpha < 0$) along with injunction case ($R > 0$), the tangential velocity is decreasing at the center of the channel and rising near the walls. Fig. 3 shows an exact opposite behavior in the case of expansion ($\alpha > 0$). In both these cases, the deviation among the curves is more prominent when the nanoparticles are not aggregating. Figs. 4 and 5 highlight the changes in tangential velocity based on the variations in permeation Reynolds number $R$. The former is for squeezing, whereas the latter is for dilation cases. As the injunction

**Table 2**
RKF and MoM result’s comparison for velocity profile, (Aggregation case).

| $\eta$ | RKF | MoM | Absolute Error |
|---|---|---|---|
| −1.0 | −0.499999998269063 | −0.500000000000000 | 1.73093728239593 e−9 |
| −0.8 | −0.443666764545050 | −0.443666766685329 | 2.14027928713278 e−9 |
| −0.6 | −0.308116096675929 | −0.308116094562113 | 2.11381578907321 e−9 |
| −0.4 | −0.128868623400056 | −0.128868636963313 | 1.35632564624011 e−8 |
| −0.2 | 0.0720033388266327 | 0.0720033394653363 | 6.38703659405770 e−10 |
| 0 | 0.280063953199712 | 0.280063970294678 | 1.70949654432206 e−8 |
| 0.2 | 0.484339147569769 | 0.484339141606658 | 5.96311011680228 e−9 |
| 0.4 | 0.674168349955648 | 0.674168341675094 | 8.28055379820114 e−9 |

**Table 3**
RKF and MoM result's comparison for temperature profile, (Aggregation case).

| $\eta$ | RKF | MoM | Absolute Error |
|---|---|---|---|
| −1.0 | 0.999999999882447 | 1.00000000000000 | 1.17553522471781 e−10 |
| −0.8 | −0.137089702911014 | −0.137174189747291 | 0.000084868362769591 |
| −0.6 | −0.625918490502684 | −0.625927348583954 | 8.85808126971366 e−10 |
| −0.4 | −0.693992872436875 | −0.694090586421631 | 0.000097139847565534 |
| −0.2 | −0.549136868647589 | −0.548662018972201 | 0.000474849675387690 |
| 0 | −0.396166594169481 | −0.396860177242529 | 0.000693583073047621 |
| 0.2 | −0.288350524076665 | −0.287619657098249 | 0.000730866978416067 |
| 0.4 | −0.204082325640286 | −0.204566293313965 | 0.000483967673678976 |

**Table 4**
RKF and MoM result's comparison for velocity profile, (non-Aggregation case).

| $\eta$ | RKF | MoM | Absolute Error |
|---|---|---|---|
| −1.0 | −0.499999997232649 | −0.500000000000000 | 2.30700453185406 e−9 |
| −0.8 | −0.444076993851173 | −0.444076996564964 | 2.71379074767708 e−9 |
| −0.6 | −0.308863283069074 | −0.308863281848754 | 1.22031906801823 e−9 |
| −0.4 | −0.129382908690677 | −0.129382921811391 | 1.31207134601574 e−8 |
| −0.2 | 0.0721946117839444 | 0.0721946117146629 | 6.92814694502886 e−11 |
| 0 | 0.281120592806166 | 0.281120608089909 | 1.52837427158659 e−8 |
| 0.2 | 0.486070513149918 | 0.486070507389484 | 5.76043401867565 e−9 |
| 0.4 | 0.676091763440645 | 0.676091755473399 | 7.96724664020587 e−9 |

**Table 5**
RKF and MoM result's comparison for temperature profile, (non-Aggregation case).

| $\eta$ | RKF | MoM | Absolute Error |
|---|---|---|---|
| −1.0 | 0.999999999866988 | 1.00000000000000 | 1.33012267866661 e−10 |
| −0.8 | −0.149368000251169 | −0.149457906723485 | 0.000089906472315 6318 |
| −0.6 | −0.636276941047703 | −0.636287638995515 | 0.000010679478117220 |
| −0.4 | −0.697582064930145 | −0.697679110059266 | 0.000097045129120 8985 |
| −0.2 | −0.547883221381597 | −0.547383177803531 | 0.000500043578065767 |
| 0 | −0.394334454672911 | −0.395064419056430 | 0.000729964383519188 |
| 0.2 | −0.287290135732765 | −0.286512522913998 | 0.000777612818766760 |
| 0.4 | −0.203489852020349 | −0.204005959054668 | 0.000516107034319035 |

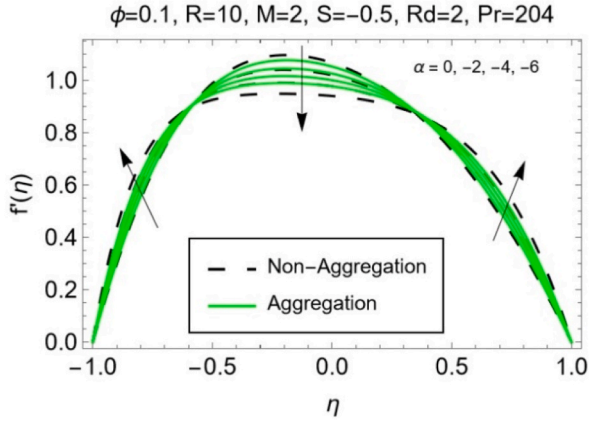


**Fig. 2.** Velocity profile for $\alpha \leq 0$.

parameter (injunction refers to the process in which fluid flow from low to the higher-pressure area) increases, the velocity values in the lower half the channel increase, and they decrease in the upper half. However, the overall values of the tangential velocity are higher for the case of expansion especially near the center of the channel.

Figs. 6 and 7 are pictured to detect the influence of magnetic strength parameter *M*. The magnetic strength parameter is a

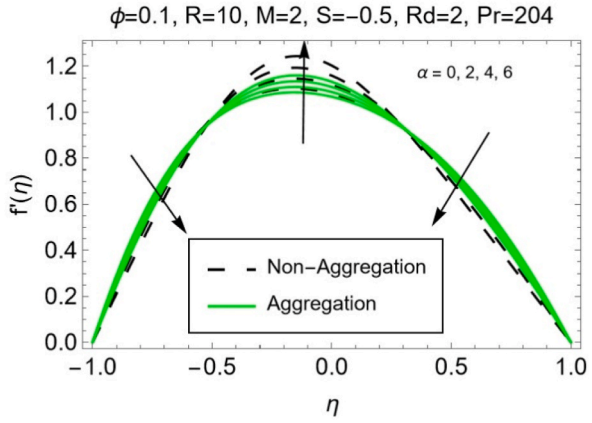


**Fig. 3.** Velocity profile for $\alpha \geq 0$.

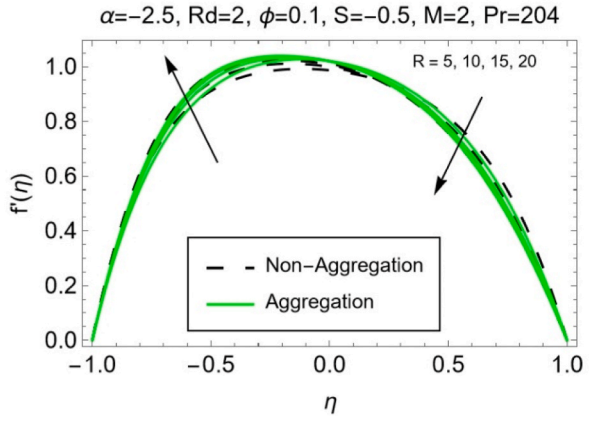


**Fig. 4.** Velocity profile for varying R, $\boldsymbol{\alpha < 0}$.

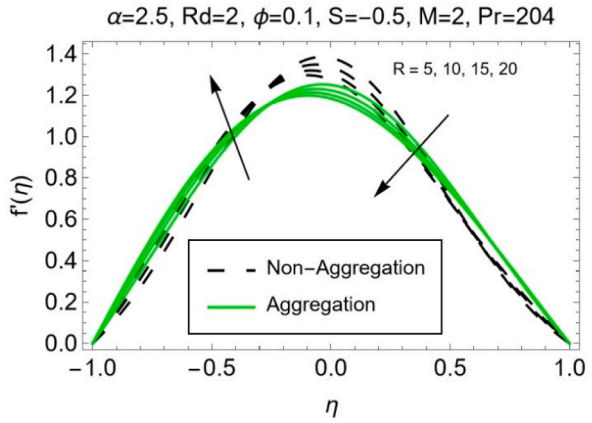


**Fig. 5.** Velocity profile for varying R, $\alpha > 0$.

dimensionless number used to describe the influence of magnetic fields on fluid flow and heat transfer. It is defined as the ratio of the magnetic force to the viscous forces in a flow and affects the tangential velocity. Fig. 6 depicts contraction together with injunction and the next considers expansion combined with injunction. Near the walls, the development of Hartmann's boundary layer is noted. In both the figures, rising the values of $M$ acceletrates the flow near the walls and do the opposite near the center. However, a slightly greater fluctuation in the velocity profile due to nanoparticle non-aggregation is seen in expansion case. The results of rising $Al_2O_3$

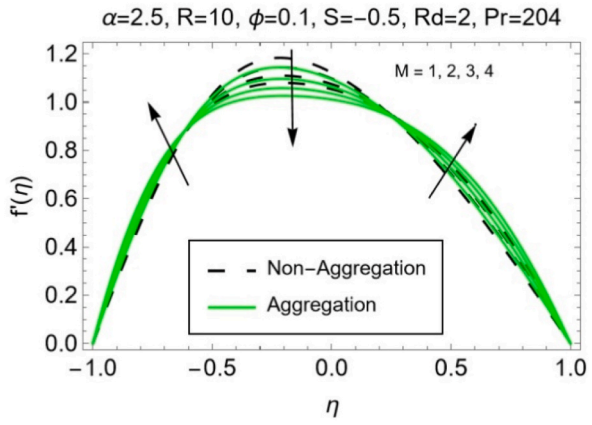


**Fig. 6.** Velocity profile for varying $M, \alpha < 0$.

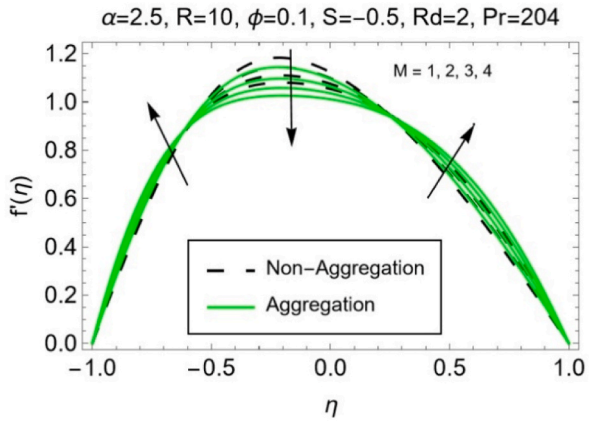


**Fig. 7.** Velocity profile for varying $M, \alpha > 0$.

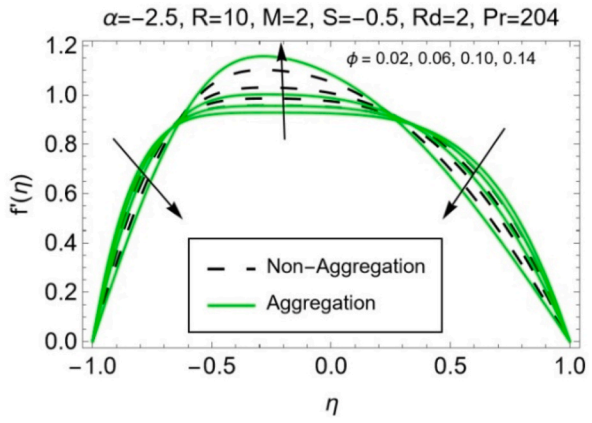


**Fig. 8.** Velocity profile for varying $\varphi, \alpha < 0$.

volume fraction φ for both squeezing and dilating cases are portrayed in Figs. 8 and 9, respectively. Enhancement in volume fraction means the addition of more nanoparticles into the base fluid. With growing $\varphi$, for contraction case, the velocity enhances in the central zone of the channel while it decreases near the walls. On the other hand, for expansion an exactly opposite behavior of the velocity is seen with lesser deviation in velocity curves compared to those of contraction scenario. Moreover, aggregation dominates in contraction while nanoparticles' non-aggregation causes faster motion of the fluid in expansion case. In Figs. 10 and 11, the impression

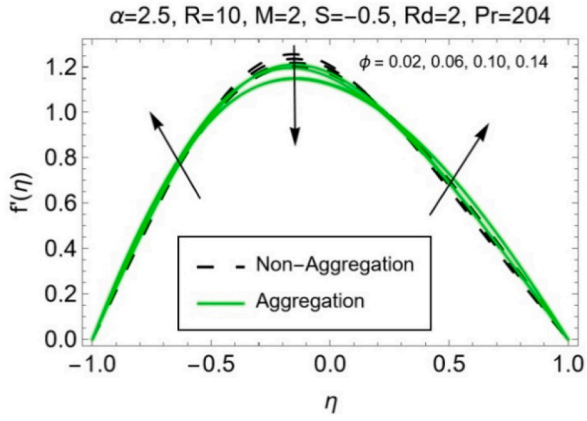


**Fig. 9.** Velocity profile for varying $\varphi, \alpha > 0$.

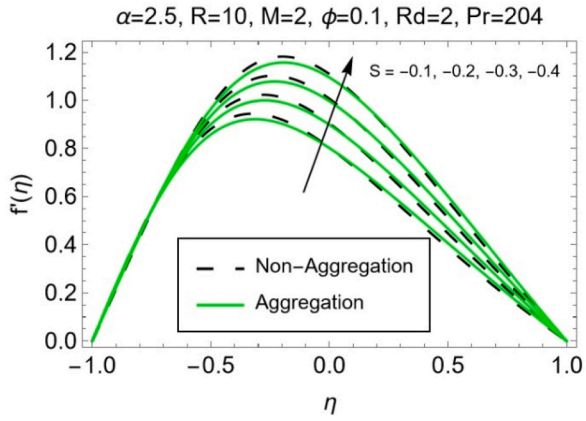


**Fig. 10.** Velocity profile for varying S, $\boldsymbol{\alpha < 0}$.

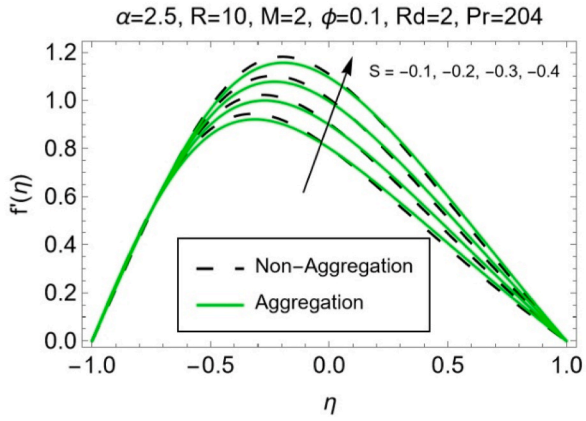


**Fig. 11.** Velocity profile for varying S , $\alpha > 0$.

of porosity parameter upon the tangential velocity is demonstrated. Porosity S is the measurement of ratio between permeation velocities of the lower and the upper walls. As the direction of the velocities is opposite, its value is considered to be negative. The results for both contraction and expansion show that the higher impact of porosity raises flow velocity a slightly higher deviation is observed for non-aggregative scenarios. The squeezing ($\alpha < 0$) and dilating ($\alpha > 0$) effects on velocity flow are discussed in Fig. 12. From the graph, it is apparent that as α increases, the tangential velocity near the walls decreases, but near the center of the channel, the opposite

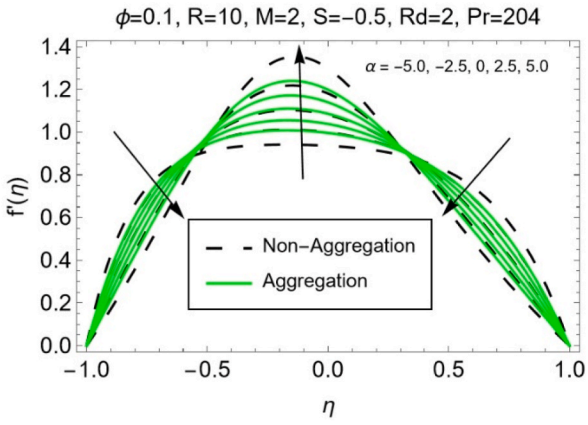


**Fig. 12.** Velocity profile for α.

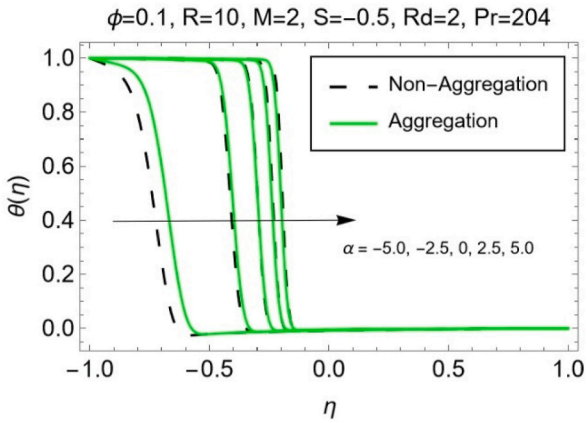


**Fig. 13.** Temperature profile for α.

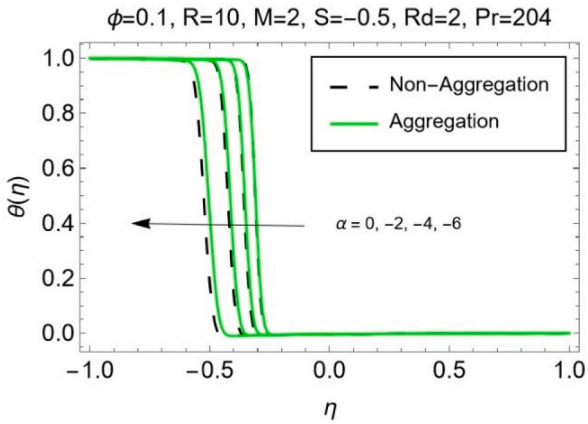


**Fig. 14.** Temperature profile for varying $\boldsymbol{\alpha} \leq 0$.

behavior is observed. The deviation in velocity curves is greater for non-aggregation than for aggregation.

After highlighting the impressions of different significant parameters on the velocity profile, we next focus on explaining how the variations in the involved parameters affect the temperature profile. In Fig. 13, we observe a thermal boundary layer near the lower wall whose thickness decreases with decreasing the values of $\alpha$, and it increases with increasing the values of the same. The phenomenon remains same for both expansion and contraction cases however a thicker boundary layer is observed for expanding channel.

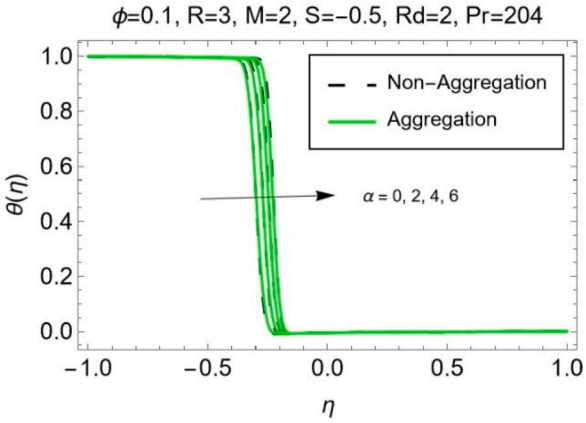


**Fig. 15.** Temperature profile for varying $\boldsymbol{\alpha} \geq 0$.

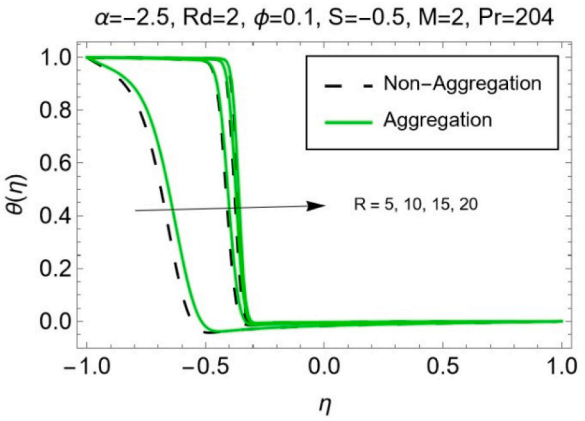


**Fig. 16.** Temperature profile for varying R , $\boldsymbol{\alpha} < \mathbf{0}$.

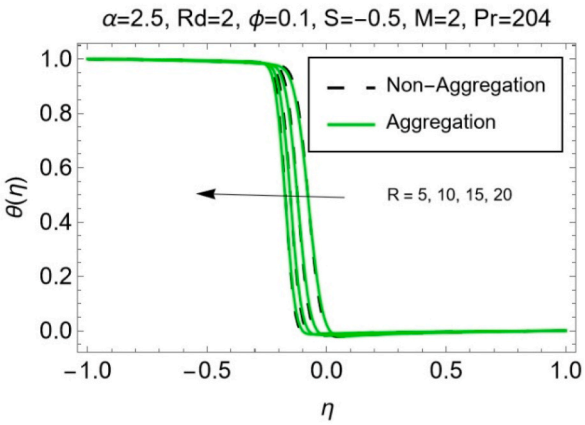


**Fig. 17.** Temperature profile for varying R , $\boldsymbol{\alpha} > \mathbf{0}$.

Moreover, for contracting channel, the boundary layer is thicker for aggregation case. For expansion however, non-aggregative fluid tends to have a thicker boundary layer. The same phenomenon is clarified more in Figs. 14 and 15. It is also worth mentioning that the case $\alpha = 0$ represents fixed parallel walls.

Figs. 16 and 17 provide insight about the temperature distribution following the increase in permeation Reynolds number $R$ for contraction and expansion cases, respectively. In former case, the thermal boundary layer thickness increases with increasing $R$; and in

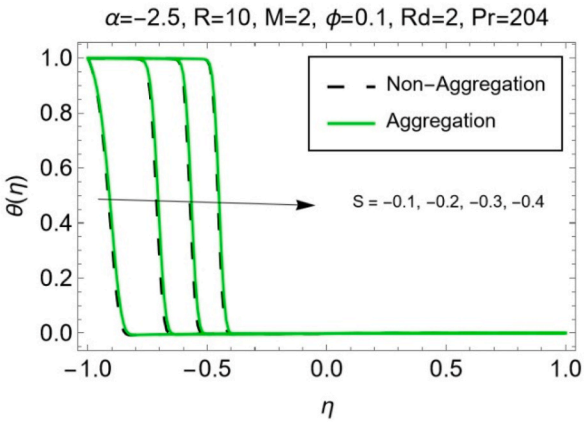


**Fig. 18.** Temperature profile for varying S , $\alpha < 0$.

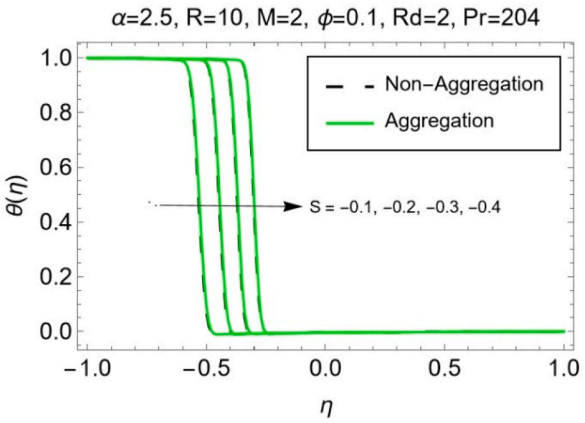


**Fig. 19.** Temperature profile for varying S , $\alpha > 0$.

the later, the phenomenon is reversed and we see a decline in thermal boundary layer thickness with increasing *R*. The boundary layer is thicker in the aggregation case as compared to the non-aggregation case.

Porosity *S* is a quantity of the measurement that defines the ratio between permeabilities of the lower and upper walls. In the next two plots (Figs. 18 and 19), the temperature profile is plotted for increasing absolute values of *S*; first is for contraction and the second is for expansion case. For both the cases, a thermal boundary layer is formed near the heated wall and the boundary layer thickness grows with increasing absolute *S*. The overall thickness remains lower in contraction case as compared to the expansion case.

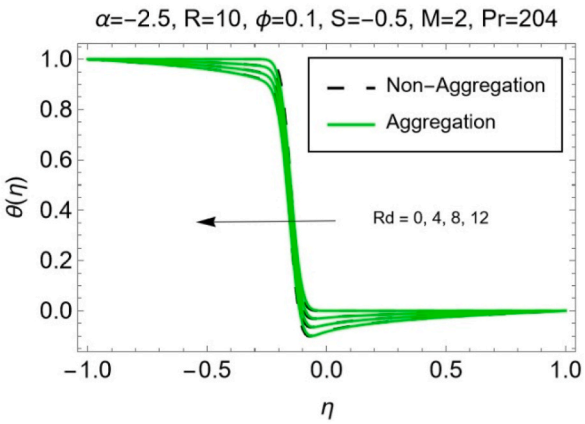


**Fig. 20.** Velocity profile for varying ***Rd***, $\alpha < 0$.

Moreover, aggregation produces slightly higher thickness in both the cases.

The radiation parameter is used to assess the significance of thermal radiation in the overall heat transfer process. It helps us determine the relative importance of radiation compared to other heat transmission mechanisms, such as convection or conduction. For example, in cases where the radiation parameter is large, thermal radiation may dominate heat transfer, and neglecting it in the analysis would lead to inaccurate understanding. By considering the radiation parameter, researchers and engineers make sure to develop more realistic models to analyze heat transfer in fluid flow problems. It leads to improved designs, optimizations, and predictions in various engineering and scientific fields. A reduction in thermal boundary layer thickness against the enhancement in radiation $Rd$ is seen in Figs. 20 and 21. Moreover, in contraction case, small pockets of visible temperature drop can be found near the center, and in the upper quarter of the lower half of the channel.

Figs. 22 and 23 represent the variation in temperature profile due to increasing nanoparticle volume fraction $\varphi$ for injection combined with contraction and expansion, respectively. At the center of channel, a smaller boost in temperature of the fluid in both contraction and expansion for increasing values of $\varphi$ is noted. It increases the thermal boundary layer thickness in both cases and the deviation among the curves is more prominent in expansion case.

The Nusselt number represents rate of heat transfer, or specifically it is called local rate of heat transfer if it is calculated on some particular points of the domain, for example at the boundaries. In Figs. 24–27 results regarding local Nusselt number for lower as well as the upper wall ($(Nu)_l$ and $(Nu)_u$, respectively) are plotted against radiation parameter $Rd$ owing to the variations in other involved parameters. Fig. 24 portrays a reduction in local rate of heat transfer at upper wall and an increment at lower wall with increasing values of $Rd$. Moreover, at higher absolute α (contraction case), the Nusselt number decreases on the upper wall and increases on the lower wall. Furthermore, the rate of change of heat transfer appears to be more sensitive to the changes in $Rd$ and $\alpha$ for aggregative case as compared to the non-aggregative case. Fig. 25 shows exactly the same behavior of Nusselt number with increasing $Rd$ but they change due to $\alpha$ is exactly oppositive to the case of contraction that we discussed in the previous figure.

Fig. 26 depicts the changes in Nusselt number at upper and lower walls due to increasing permeation Rynolds number $R$ and radiation parameter $Rd$. Increase in radiation increases absolute rate of heat transfer at both the walls. The effect of increasing $R$ is adverse and we see a decline in absolute rate of heat transfer at both the walls. Fig. 27 describes the deviation in local rate of heat transfer against $Rd$, upon decreasing the porosity parameter S. With decreasing $S$, absolute local rate of heat transfer decreases at both the walls. Moreover, it's worth mentioning that for all the cases aggregation bears higher values for absolute Nusselt number.

## 5. Conclusion

This manuscript analyzes the flow of ethylene glycol-based aluminum oxide nanofluid through a rectangular channel with contracting and expanding permeable walls. The flow is influenced by thermal radiation and a constant magnetic field. The effects of nanoparticle aggregation and non-aggregation are also considered. The Method of Moments is utilized to solve the mathematical equations associated with the flow model. The solution was sought to analyze the variations in the velocity and temperature profiles due to the changes in involved dimensionless parameters. Results were presented in the form of tables and plots accompanied by suitable explanations and discussion.

The key findings of the research are as follows:

- The absolute errors, which were found to be as low as $10^{-11}$ in certain cases, offer a comprehensive comparison between the outcomes obtained from Method of Moments (MoM) and the Runge Kutta Fehlberg algorithm.
- Contraction of the channel leads to faster flow near the walls and decreases the flow at the center, while expansion shows the opposite behavior with a reserved pattern for tangential velocity.

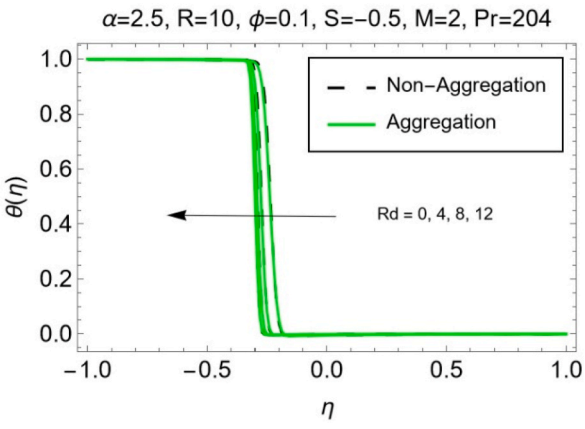


**Fig. 21.** Velocity profile for varying $Rd, \alpha > 0$.

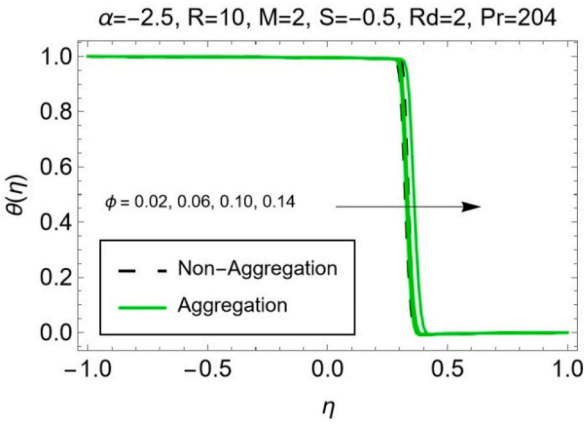


**Fig. 22.** Velocity profile for varying $\boldsymbol{\varphi}, \boldsymbol{\alpha} < \mathbf{0}$.

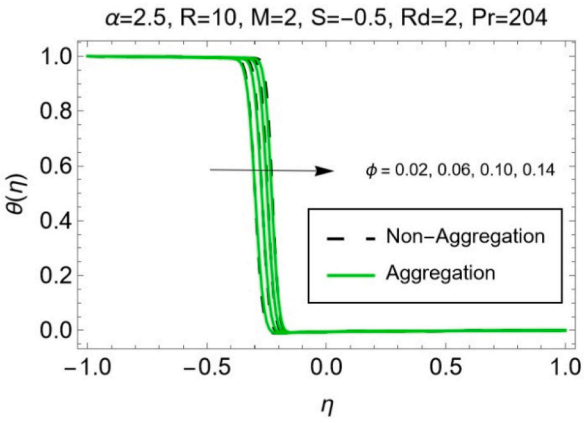


**Fig. 23.** Velocity profile for varying $\boldsymbol{\varphi}, \boldsymbol{\alpha} > 0$.

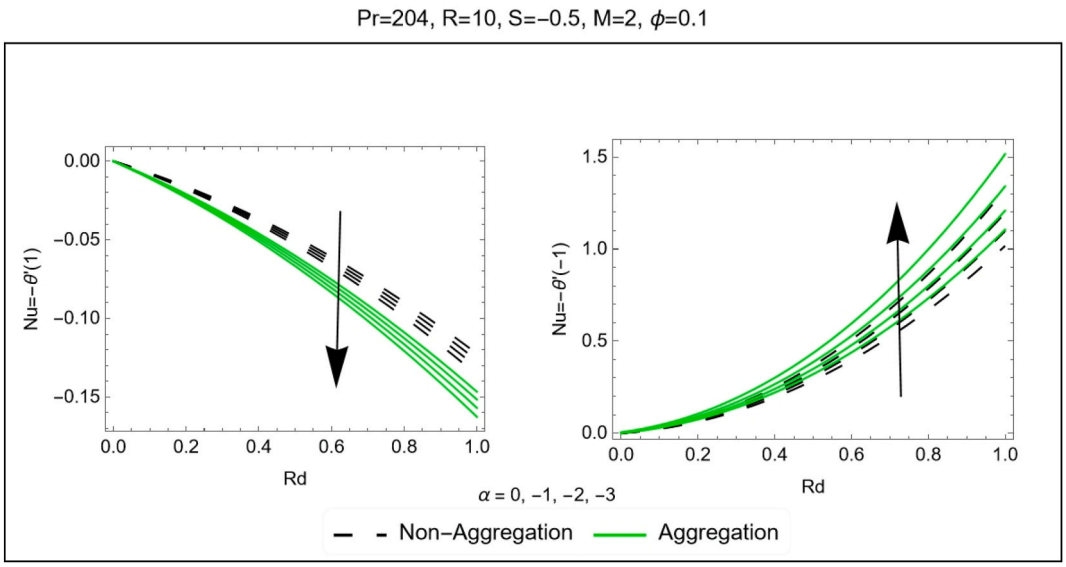


**Fig. 24.** Nusselt number upon $\boldsymbol{\alpha} \leq 0$ with $\boldsymbol{R} > 0$.

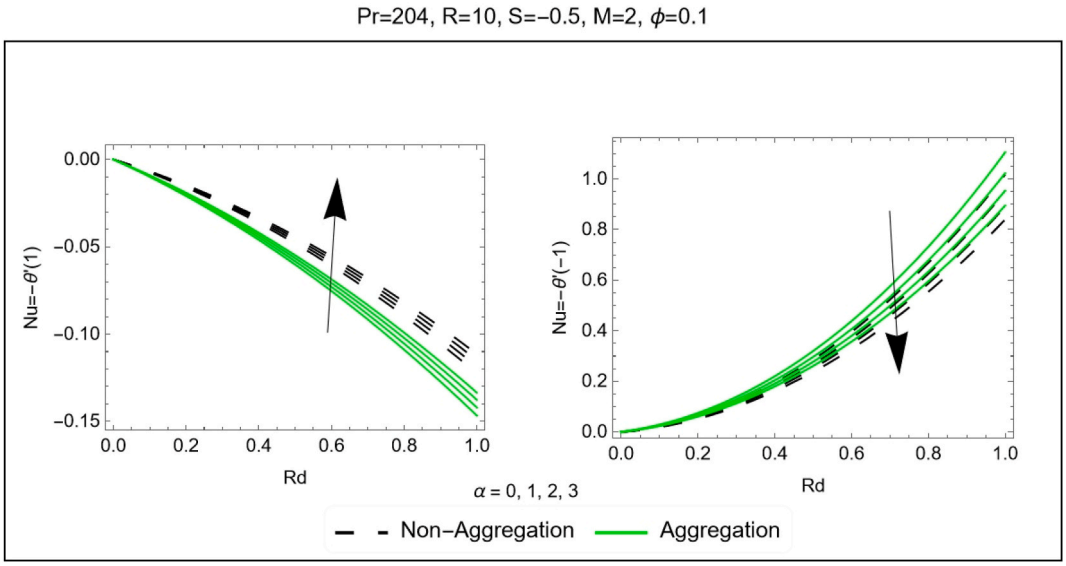


**Fig. 25.** Nusselt number upon $\boldsymbol{\alpha} \geq 0$ with $\boldsymbol{R} > 0$.

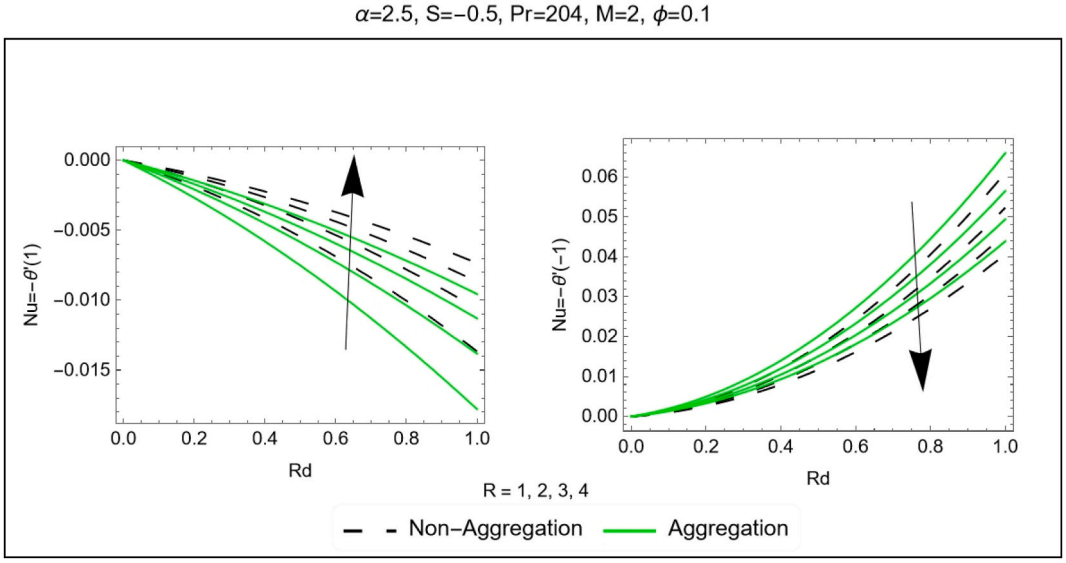


**Fig. 26.** Nusselt number upon with $\boldsymbol{R}, \alpha > 0$.

- The presence of permeable walls affects the velocity profile, increasing the velocity at the lower walls and decreasing it at the upper walls. However, the effect is negligible near the origin for contraction and near the ending walls for expansion.
- A Hertzman boundary layer is observed in both contracting and expanding walls, where the tangential velocity slows down in the central section compared to the walls.
- Increasing the volumetric fraction of nanoparticles enhances the velocity profile near the center of the channel for contraction, while the opposite effect is observed for expansion.
- The absolute porosity parameter has a positive impact on the velocity flow, meaning that increasing $S$ leads to higher velocities in both contraction and expansion scenarios.
- The temperature in the center of the channel decreases for contraction and increases for expansion, while the temperature at the walls remains unchanged in both cases.
- With an increase in the values of $R$, the temperature in the central region rises due to contraction and it reverse for expansion, leaving the walls unaffected in both contraction and expansion.
- The temperature of the nanolubricant is higher by the hike in absolute values of porosity constraint $S$.
- A fall in temperature profile is evident for rise in thermal radiation.

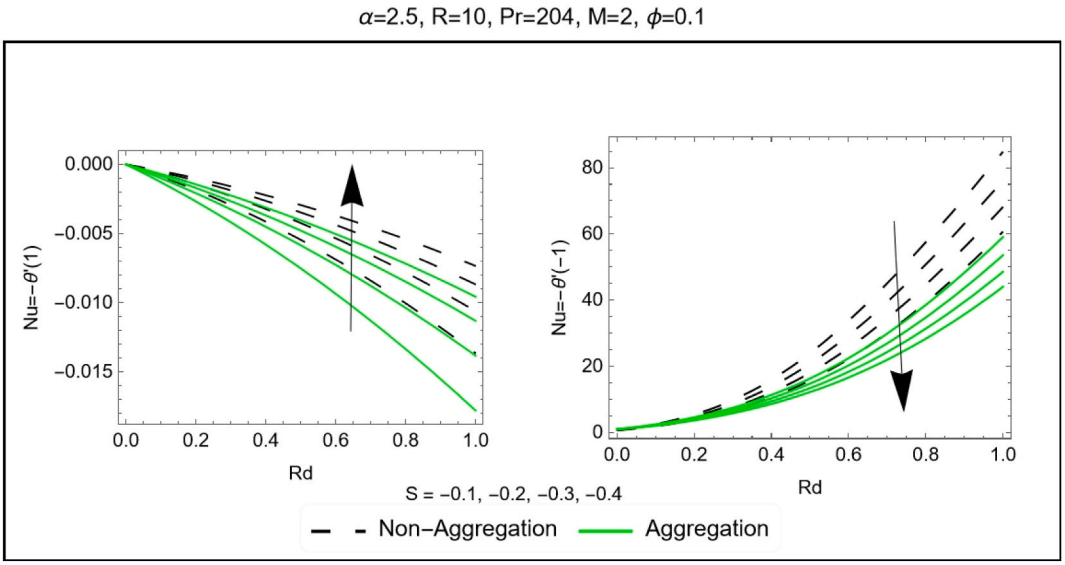


**Fig. 27.** Nusselt number upon $S$ with $\alpha > 0$ and $R > 0$.

- A slight growth in temperature of nanolubricant is noted following the rise in volumetric fraction of nanoparticles.
- The velocity curves with nanoparticles aggregation have comparatively lesser deviation than the non-aggregation one.
- For lesser values of α in contraction and for small $R$ temperature decline faster in non-aggregation, however the aggregation development has almost negligible effect on temperature profile for the rest parameters.

While providing valuable insights, the study's limitations include simplifications in the model, homogeneous nanoparticle dispersion assumption, limited thermal radiation model, and constant material properties assumption. Future research opportunities lie in exploring turbulent flow regimes, developing advanced nanoparticle aggregation models, considering temperature-dependent material properties, conducting experimental validation, performing optimization studies, and exploring multi-physics effects. In future more generalized models can be established on the basis of the current model which would try to minimize the simplification assumptions.

## Funding statement

The authors have no funding available.

## Data availability statement

All the data is already a part of this manuscript.

## CRediT authorship contribution statement

**Noor Muhammad:** Formal analysis, Software, Validation, Visualization, Writing – original draft. **Naveed Ahmed:** Conceptualization, Investigation, Methodology, Supervision, Validation, Writing – review & editing.

## Declaration of competing interest

The authors declare that they have no known competing financial interests or personal relationships that could have appeared to influence the work reported in this paper.

## References

[1] S. Uchida, H. Aoki, Unsteady flows in a semi-infinite contracting or expanding pipe, J. Fluid Mech. 82 (2) (Sep. 1977) 371–387, https://doi.org/10.1017/S0022112077000718.
[2] M. Goto, S. Uchida, Unsteady flows in a semi-infinite expanding pipe with injection through wall, J. Jpn. Soc. Aeronaut. Space Sci. 38 (434) (1990) 131–138, https://doi.org/10.2322/jjsass1969.38.131.
[3] E. Dauenhauer, J. Majdalani, Unsteady flows in semi-infinite expanding channels with wall injection, in: 30th Fluid Dynamics Conference, Reston, Virigina: American Institute of Aeronautics and Astronautics, Jun, 1999, https://doi.org/10.2514/6.1999-3523.

[4] J. Majdalani, C. Zhou, C.A. Dawson, Two-dimensional viscous flow between slowly expanding or contracting walls with weak permeability, J. Biomech. 35 (10) (Oct. 2002) 1399–1403, https://doi.org/10.1016/S0021-9290(02)00186-0.

[5] R.K. Bhatnagar, Fluctuating flow of a viscoelastic fluid in a porous channel, J. Appl. Mech. 46 (1) (Mar. 1979) 21–25, https://doi.org/10.1115/1.3424507.

[6] J. Majdalani, C. Zhou, Moderate-to-large injection and suction driven channel flows with expanding or contracting walls, Z. Angew. Math. Mech. 83 (3) (Mar. 2003) 181–196, https://doi.org/10.1002/zamm.200310018.

[7] N. Ahmed, U. Khan, S.T. Mohyud-Din, B. Bin-Mohsin, A finite element investigation of the flow of a Newtonian fluid in dilating and squeezing porous channel under the influence of nonlinear thermal radiation, Neural Comput. Appl. 29 (2) (Jan. 2018) 501–508, https://doi.org/10.1007/s00521-016-2463-9.

[8] N. Muhammad, N. Ahmed, Subdomain method for unsteady flow of ZnO − SAE50 nano-lubricant through expanding/contracting walls in an asymmetric porous horizontal channel, Int. Commun. Heat Mass Tran. 138 (Nov. 2022), 106410, https://doi.org/10.1016/j.icheatmasstransfer.2022.106410.

[9] S.U.S. Choi, J.A. Eastman, Enhancing Thermal Conductivity of Fluids with Nanoparticles, 1995.

[10] Y. Xuan, Q. Li, Investigation on convective heat transfer and flow features of nanofluids, J. Heat Tran. 125 (1) (Feb. 2003) 151–155, https://doi.org/10.1115/1.1532008.

[11] J. Buongiorno, Convective transport in nanofluids, J. Heat Tran. 128 (3) (Mar. 2006) 240–250, https://doi.org/10.1115/1.2150834.

[12] U. Khan, N. Ahmed, S.T. Mohyud-Din, B. Bin-Mohsin, Nonlinear radiation effects on MHD flow of nanofluid over a nonlinearly stretching/shrinking wedge, Neural Comput. Appl. 28 (8) (Aug. 2017) 2041–2050, https://doi.org/10.1007/s00521-016-2187-x.

[13] M. Basit Shafiq, et al., Thermal performance enhancement of shell and helical coil heat exchanger using MWCNTs/water nanofluid, J. Therm. Anal. Calorim. 147 (21) (Nov. 2022) 12111–12126, https://doi.org/10.1007/s10973-022-11405-5.

[14] M. Bagheri Motlagh, M. Kalteh, Molecular dynamics simulation of nanofluid convective heat transfer in a nanochannel: effect of nanoparticles shape, aggregation and wall roughness, J. Mol. Liq. 318 (2020), 114028, https://doi.org/10.1016/j.molliq.2020.114028. Nov.

[15] K. Swain, B. Mahanthesh, Thermal enhancement of radiating magneto-nanoliquid with nanoparticles aggregation and joule heating: a three-dimensional flow, Arabian J. Sci. Eng. 46 (6) (Jun. 2021) 5865–5873, https://doi.org/10.1007/s13369-020-04979-5.

[16] B. Mahanthesh, Flow and heat transport of nanomaterial with quadratic radiative heat flux and aggregation kinematics of nanoparticles, Int. Commun. Heat Mass Tran. 127 (Oct. 2021), 105521, https://doi.org/10.1016/j.icheatmasstransfer.2021.105521.

[17] A. Sabu, J. Mackolil, B. Mahanthesh, A. Mathew, Nanoparticle aggregation kinematics on the quadratic convective magnetohydrodynamic flow of nanomaterial past an inclined flat plate with sensitivity analysis, Proc. IME E J. Process Mech. Eng. 236 (3) (Jun. 2022) 1056–1066, https://doi.org/10.1177/09544089211056235.

[18] F. Wang, et al., The effects of nanoparticle aggregation and radiation on the flow of nanofluid between the gap of a disk and cone, Case Stud. Therm. Eng. 33 (May 2022), 101930, https://doi.org/10.1016/j.csite.2022.101930.

[19] F. Wang, et al., Aspects of uniform horizontal magnetic field and nanoparticle aggregation in the flow of nanofluid with melting heat transfer, Nanomaterials 12 (6) (2022) 1000, https://doi.org/10.3390/nano12061000. Mar.

[20] L. Th Benos, E.G. Karvelas, I.E. Sarris, Crucial effect of aggregations in CNT-water nanofluid magnetohydrodynamic natural convection, Therm. Sci. Eng. Prog. 11 (Jun. 2019) 263–271, https://doi.org/10.1016/j.tsep.2019.04.007.

[21] P. Sunthrayuth, et al., Impact of nanoparticle aggregation on heat transfer phenomena of second grade nanofluid flow over melting surface subject to homogeneous-heterogeneous reactions, Case Stud. Therm. Eng. 32 (Apr. 2022), 101897, https://doi.org/10.1016/j.csite.2022.101897.

[22] N. Acharya, K. Das, P.K. Kundu, Effects of aggregation kinetics on nanoscale colloidal solution inside a rotating channel, J. Therm. Anal. Calorim. 138 (1) (Oct. 2019) 461–477, https://doi.org/10.1007/s10973-019-08126-7.

[23] R. Ellahi, M. Hassan, A. Zeeshan, Aggregation effects on water base $Al_2O_3$ -nanofluid over permeable wedge in mixed convection, Asia Pac. J. Chem. Eng. 11 (2) (Mar. 2016) 179–186, https://doi.org/10.1002/apj.1954.

[24] J. Mackolil, B. Mahanthesh, Inclined magnetic field and nanoparticle aggregation effects on thermal Marangoni convection in nanoliquid: a sensitivity analysis, Chin. J. Phys. 69 (Feb. 2021) 24–37, https://doi.org/10.1016/j.cjph.2020.11.006.

[25] J. Mackolil, B. Mahanthesh, Sensitivity analysis of Marangoni convection in TiO2–EG nanoliquid with nanoparticle aggregation and temperature-dependent surface tension, J. Therm. Anal. Calorim. 143 (3) (2021) 2085–2098, https://doi.org/10.1007/s10973-020-09642-7. Feb.

[26] M. Kothandapani, J. Prakash, Effects of thermal radiation parameter and magnetic field on the peristaltic motion of Williamson nanofluids in a tapered asymmetric channel, Int. J. Heat Mass Tran. 81 (Feb. 2015) 234–245, https://doi.org/10.1016/j.ijheatmasstransfer.2014.09.062.

[27] P.V. Satya Narayana, Effects of variable permeability and radiation absorption on magnetohydrodynamic (MHD) mixed convective flow in a vertical wavy channel with traveling thermal waves, Propulsion and Power Research 4 (3) (Sep. 2015) 150–160, https://doi.org/10.1016/j.jppr.2015.07.002.

[28] N. Ahmed, U. Khan, S.T. Mohyud-Din, Influence of nonlinear thermal radiation on the viscous flow through a deformable asymmetric porous channel: a numerical study, J. Mol. Liq. 225 (Jan. 2017) 167–173, https://doi.org/10.1016/j.molliq.2016.11.021.

[29] M.A. Kumar, Y.D. Reddy, B.S. Goud, V.S. Rao, Effects of soret, dufour, hall current and rotation on MHD natural convective heat and mass transfer flow past an accelerated vertical plate through a porous medium, International Journal of Thermofluids 9 (Feb. 2021), 100061, https://doi.org/10.1016/j.ijft.2020.100061.

[30] U. Adnan, Khan, N. Ahmed, I. Khan, A. Mohamed, S. Mehrez, Heat transfer evaluation in MgZn6Zr/C8H18 [(Magnesium–Zinc–Zirconium)/Engine oil] with non-linear solar thermal radiations and modified slip boundaries over a 3-dimensional convectively heated surface, Front. Energy Res. 10 (Apr) (2022), https://doi.org/10.3389/fenrg.2022.867734.

[31] A. Saha, N.K. Manna, K. Ghosh, N. Biswas, Analysis of geometrical shape impact on thermal management of practical fluids using square and circular cavities, Eur. Phys. J. Spec. Top. 231 (13–14) (Sep. 2022) 2509–2537, https://doi.org/10.1140/epjs/s11734-022-00593-8.

[32] A. Saha, A. Chakravarty, K. Ghosh, N. Biswas, N.K. Manna, Role of Obstructing Block on Enhanced Heat Transfer in a Concentric Annulus," *Waves In Random and Complex Media*, 2022, pp. 1–25, https://doi.org/10.1080/17455030.2022.2106386. Aug.

[33] M. Mustafa, J.A. Khan, T. Hayat, A. Alsaedi, Buoyancy effects on the MHD nanofluid flow past a vertical surface with chemical reaction and activation energy, Int. J. Heat Mass Tran. 108 (May 2017) 1340–1346, https://doi.org/10.1016/j.ijheatmasstransfer.2017.01.029.

[34] M. Mustafa, J.A. Khan, T. Hayat, A. Alsaedi, Buoyancy effects on the MHD nanofluid flow past a vertical surface with chemical reaction and activation energy, Int. J. Heat Mass Tran. 108 (May 2017) 1340–1346, https://doi.org/10.1016/j.ijheatmasstransfer.2017.01.029.

[35] M.K. Nayak, MHD 3D flow and heat transfer analysis of nanofluid by shrinking surface inspired by thermal radiation and viscous dissipation, Int. J. Mech. Sci. 124 (125) (May 2017) 185–193, https://doi.org/10.1016/j.ijmecsci.2017.03.014.

[36] M.K. Nayak, MHD 3D flow and heat transfer analysis of nanofluid by shrinking surface inspired by thermal radiation and viscous dissipation, Int. J. Mech. Sci. 124 (125) (May 2017) 185–193, https://doi.org/10.1016/j.ijmecsci.2017.03.014.

[37] N. Ahmed, A. Abbasi, F. Saba, U. Khan, S.T. Mohyud-Din, Flow of ferro-magnetic nanoparticles in a rotating system: a numerical investigation of particle shapes, Indian J. Phys. 92 (8) (2018) 969–977, https://doi.org/10.1007/s12648-018-1186-4. Aug.

[38] F. Rehman, M.I. Khan, M. Sadiq, A. Malook, MHD flow of carbon in micropolar nanofluid with convective heat transfer in the rotating frame, J. Mol. Liq. 231 (Apr. 2017) 353–363, https://doi.org/10.1016/j.molliq.2017.02.022.

[39] D. Chatterjee, N. Biswas, N.K. Manna, D. Kumar Mandal, A.J. Chamkha, Magneto-nanofluid flow in cylinder-embedded discretely heated-cooled annular thermal systems: conjugate heat transfer and thermodynamic irreversibility, J. Magn. Magn Mater. 569 (Mar. 2023), 170442, https://doi.org/10.1016/j.jmmm.2023.170442.

[40] D. Chatterjee, N. Biswas, N.K. Manna, S. Sarkar, Effect of discrete heating-cooling on magneto-thermal-hybrid nanofluidic convection in cylindrical system, Int. J. Mech. Sci. 238 (Jan. 2023), 107852, https://doi.org/10.1016/j.ijmecsci.2022.107852.

[41] Adnan, et al., Impact of freezing temperature (Tfr) of Al2O3 and molecular diameter (H2O)d on thermal enhancement in magnetized and radiative nanofluid with mixed convection, Sci. Rep. 12 (1) (2022) 703, https://doi.org/10.1038/s41598-021-04587-9. Jan.

[42] S. Hosseini, F. Farahbod, The study of effective of added aluminum oxide nano particles to the drilling fluid: the evaluation of two synthesis methods, J. Petrol Environ. Biotechnol. 7 (3) (2016), https://doi.org/10.4172/2157-7463.1000283.

[43] H. Maddah, M. Rezazadeh, M. Maghsoudi, S. NasiriKokhdan, The effect of silver and aluminum oxide nanoparticles on thermophysical properties of nanofluids, J Nanostructure Chem 3 (1) (2013) 28, https://doi.org/10.1186/2193-8865-3-28. Dec.
[44] H. Yue, Y. Zhao, X. Ma, J. Gong, Ethylene glycol: properties, synthesis, and applications, Chem. Soc. Rev. 41 (11) (2012) 4218, https://doi.org/10.1039/c2cs15359a.
[45] R. Cortell, Fluid flow and radiative nonlinear heat transfer over a stretching sheet, J. King Saud Univ. Sci. 26 (2) (Apr. 2014) 161–167, https://doi.org/10.1016/j.jksus.2013.08.004.
[46] M. Bilal, H. Arshad, M. Ramzan, Z. Shah, P. Kumam, Unsteady hybrid-nanofluid flow comprising ferrousoxide and CNTs through porous horizontal channel with dilating/squeezing walls, Sci. Rep. 11 (1) (Jun. 2021), 12637, https://doi.org/10.1038/s41598-021-91188-1.
[47] S. Uchida, H. Aoki, Unsteady flows in a semi-infinite contracting or expanding pipe, J. Fluid Mech. 82 (2) (Sep. 1977) 371–387, https://doi.org/10.1017/S0022112077000718.
[48] A. Abbasi, et al., Optimized analysis and enhanced thermal efficiency of modified hybrid nanofluid (Al2O3, CuO, Cu) with nonlinear thermal radiation and shape features, Case Stud. Therm. Eng. 28 (Dec. 2021), 101425, https://doi.org/10.1016/j.csite.2021.101425.
[49] L. Desvillettes, Some applications of the method of moments for the homogeneous Boltzmann and Kac equations, Arch. Ration. Mech. Anal. 123 (4) (1993) 387–404, https://doi.org/10.1007/BF00375586.
[50] G.S. Denicol, D.H. Rischke, Fluid Dynamics from the Method of Moments, 2021, pp. 213–254, https://doi.org/10.1007/978-3-030-82077-0_8.
[51] G.S. Rocha, G.S. Denicol, Transient fluid dynamics with general matching conditions: a first study from the method of moments, Phys. Rev. D 104 (9) (Nov. 2021), 096016, https://doi.org/10.1103/PhysRevD.104.096016.
[52] B.A. Finlayson, The Method of Weighted Residuals and Variational Principles, Society for Industrial and Applied Mathematics, Philadelphia, PA, 2013, https://doi.org/10.1137/1.9781611973242.